THREE-DIMENSIONAL THERMO-PORO-MECHANICAL MODELING OF RESERVOIR STIMULATION AND INDUCED MICROSEISMICITY IN GEOTHERMAL RESERVOIR

Sang Hoon Lee and Ahmad Ghassemi

Department of Petroleum Engineering, Texas A&M University
3116 TAMU 507 Richardson Building
College Station, TX, 77845, USA
e-mail: ahmad.ghassemi@pe.tamu.edu

ABSTRACT

Analysis of stress change and permeability variations caused by rock failure is much interest in geothermal reservoir. Cold water injection into the reservoir can cause significant change of pore pressure, temperature, and the stress state in the hot reservoir which in turn impact rock permeability. Analysis of this process is useful in designing geothermal reservoirs. In view of the complexity of the process, numerical modeling is generally necessary. In this paper, we present a three-dimensional fully-coupled thermo-poro-mechanical finite element model with damage mechanics to simulate reservoir stimulation by hydraulic fracturing. The model considers stress-dependent permeability, and convective heat transport in the thermo-poroelastic formulation. Rock damage is reflected in the alteration of elastic modulus and permeability. A series of numerical experiments have been carried out to study the impact of cold water injection on the reservoir. Results show different patterns of damage localization around the wellbore and its propagation into the reservoir under different stress regime. In addition to the geometry of the stimulated zone, locations of potential induced-seismicity caused by injection are calculated, and show qualitative agreement observations in the field. The model provides a useful tool for the analysis of stress induced micro-seismicity and fracture propagations in geothermal and petroleum reservoirs.

INTRODUCTION

Water injection in geothermal reservoir involves coupled rock deformation and fluid flow as described in Biot's poroelastic theory [1]. Thermal and chemical effects can also be significant in this context [2]. The influence of fluid flow and temperature change around the wellbore on the stress variations in the reservoir can be described using thermo-poroelasticity. This influence is often computed based on a linear rock behavior without rock failure. The assumptions of linear elastic rock skeleton and constant permeability have limitations for use in predicting the real behavior of the reservoir rock. Generally, the strain-stress behavior of rocks in triaxial tests shows hardening and post-peak softening. This behavior depends on the rock type, pore pressure, stress conditions, and temperature. The continuum damage mechanics approach is one of the methods that can capture the hardening and softening behavior of the rock. The continuum damage mechanics was first introduced by Kachanov and since has been developed by many researchers [3-8] who have investigated inelastic behavior caused by crack initiation, micro-void growth, and fracture propagation. Also, the evolution of rock damage in the presence of poroelastic and thermo-poroelastic effects has been considered. Selvadurai [8] studied influence of damage and permeability in porous rock. His results showed a significant permeability alteration caused by damage evolution in consolidation problems. Tang et al. proposed a damage and permeability model based on experimental strain-stress observations and permeability measurements [6-7]. The permeability variations induced by altered stress and rock failure has been studied by many researchers [e.g., 9-12], and relations have been suggested between permeability change and micro-crack and void evolution [12] showing that for granite permeability can increase by a factor of four. Other studies present different magnitudes for the increase in the level of permeability depending on rock type and experimental conditions.

In this work, we present the development of a finite element model to study the influence of thermo-poro-mechanical coupling on rock damage evolution and permeability variation. The damage model used corresponds to the brittle rock failure behavior with crack initiation, micro-void growth and permanent deformation prior to fracture. In order to capture the full effects of rock cooling by injection in the presence of higher fluid fluxes caused by rock degradation and permeability enhancement, the model considers both the conductive and convective heat transfer in porous medium. Numerical

simulations are presented to verify the model and to illustrate the role of various mechanisms in rock fracture and distributed damage evolution during stimulation.

THERMO-POROELASTIC MODEL

The theory of thermo-poroelasticity (or poro-thermoelasticity) is developed by combining the influence of thermal stress and differential solid/fluid expansion to rock stresses and fluid diffusion.

Governing Equations

The governing equations include the constitutive and transport laws. The constitutive equations of thermo-poroelasticity have been developed by McTigue [13] and Palciauskas and Domenico [14]. Using the geomechanics sign convention of compression positive, the constitutive equations are:

$$\dot{\sigma}_{ij} = 2G\dot{\varepsilon}_{ij} + \left(K - \frac{2G}{3}\right)\dot{\varepsilon}_{kk}\delta_{ij} + \alpha \dot{p}\delta_{ij} + \gamma_1\dot{T}\delta_{ij} \quad (1)$$

$$\dot{\zeta} = \alpha\dot{\varepsilon}_{ii} + \beta\dot{p} - \gamma_2\dot{T} \quad (2)$$

where σ_{ij} and ε_{ij} are the total stress and strain tensors, p and T are the pore pressure and temperature respectively. α is the Biot coefficient, ζ is the variation of fluid contents, K is bulk modulus, and G is the shear modulus; γ_1, γ_2 and β are given by:

$$\beta = \frac{\alpha - \varphi}{K_s} + \frac{\varphi}{K_f} \quad (3)$$

$$\gamma_1 = K\alpha_m \quad (4)$$

$$\gamma_2 = \alpha\alpha_m + \left(\alpha_f - \alpha_m\right)\phi \quad (5)$$

where ϕ is the porosity, α_f and α_m the thermal expansion coefficients of solid and fluid, respectively.

Fluid flow in porous rock is governed by Darcy's law, and heat conduction obeys Fourier's law, so that:

$$J^f = -\rho_f \frac{k}{\eta}\nabla p \quad (6)$$

$$J^T = -k^T\nabla T \quad (7)$$

where ρ_f is fluid mass density, k and η the permeability and viscosity, respectively, k^T the thermal conductivity.

The balance of force and continuity for the fluid mass are given by:

$$\sigma_{ij,j} = 0 \quad (8)$$

$$\frac{\partial\zeta}{\partial t} = -\frac{1}{\rho_f}\nabla J^f \quad (9)$$

By substituting the constitutive equations into the balance equations given by Eqn. (8), (9), we obtain the field equations for the rock deformation and fluid flow, namely Eqn. (10) and Eqn. (11). The conservation of energy with Fourier's law yields the field equation for the temperature distribution:

$$\left(K + \frac{G}{3}\right)\nabla(\nabla \cdot u) + G\nabla^2 u + m(\alpha\nabla p + \gamma_1\nabla T) = 0 \quad (10)$$

$$\alpha(\nabla \cdot \dot{u}) + \beta\dot{p} - \frac{k}{\eta}\nabla^2 p - \gamma_2\dot{T} = 0 \quad (11)$$

$$\dot{T} + v(\nabla T) - c^T\nabla^2 T = 0 \quad (12)$$

where u is the displacement and $m = [1, 1, 1, 0, 0, 0]^T$ for three-dimensional cases. In Eqn. (12), we consider convective heat transfer because of cooling effects which are from increased flow velocity in damage phase. This fluid velocity is coupled with pore pressure variations in Darcy's law,

$$v = -\frac{k}{\eta}\nabla p.$$

DAMAGE AND PERMEABILITY MODEL

We use a model of rock damage and permeability as proposed by Tang et al. based on experiments [6, 7]. The model is modified herein to consider continuous stress relaxation from the peak stress to the residual strength (softening regime). According to this model, the strain-stress behavior of rock can be divided into an elastic phase and a damage phase. In the elastic phase there is no damage in the rock, whereas the rock begins to fail by crack initiation, crack-growth and void-growth when the stress conditions reach the failure level i.e., they satisfy the failure criterion. An elastic-damage mechanics represents the rock degradation by expressing the damage in terms of a reduction on the elastic modulus as the damage proceeds:

$$E = (1-d)E_0 \quad (13)$$

where d represents the internal damage variable describing the amount of degradation (crack initiation, micro-void growth and crack propagation) and E_0 is the initial rock modulus. If damage occurs by compressive stress, the damage variable is defined in terms of strain, peak stress, and residual compressive strength of the rock as:

$$d = 1 - \left[\left(\frac{f_{cr} - f_c}{\varepsilon_{cr} - \varepsilon_c}\right)(\varepsilon - \varepsilon_c) + f_c\right]\Big/E_0\varepsilon \quad (14)$$

$$(\varepsilon_c < \varepsilon < \varepsilon_{cr})$$

$$d = 1 - \frac{f_{cr}}{E_0 \bar{\varepsilon}} \qquad (\varepsilon > \varepsilon_{cr}) \qquad (15)$$

where f_{cr} and ε_{cr} are the residual compressive strength and strain, and f_c and ε_r are the peak stress and strain in compressive field. $\bar{\varepsilon}$ is the equivalent strain.

If damage evolves in a tensile stress field, the damage variable is defined using the residual tensile strength of the rock as:

$$d = 1 - \frac{f_{tr}}{E_0 \bar{\varepsilon}} \qquad (\varepsilon > \varepsilon_{tr}) \qquad (16)$$

where f_{tr} and ε_{tr} are the residual tensile strength and strain, respectively.

To trace the progress of damage under shear or tensile stress, a Mohr-Coulomb failure criterion is used:

$$F = \frac{\sigma_1 + \sigma_3}{2} \sin \phi_f - \frac{\sigma_1 - \sigma_3}{2} - c_f \cos \phi_f \qquad (17)$$

where σ_1 and σ_3 are the maximum and minimum principal stresses, respectively; ϕ_f and c_f represent the friction angle and cohesion, respectively.

The rock permeability model used also considers altered permeability in the elastic and damage phase [6, 7]:

$$k = k_0 e^{-\beta_d (\sigma_{ii}/3 - \alpha p)} \qquad (d = 0) \qquad (18)$$

$$k = \zeta_d k_0 e^{-\beta_d (\sigma_{ii}/3 - \alpha p)} \qquad (0 < d \leq 1) \qquad (19)$$

where k_0 is the initial permeability, ζ_d and β_d are material constants determined empirically. Here ζ_d ($\zeta_d > 1$) indicates permeability increase by damage. The parameter β_d [Pa^{-1}] in the exponent term is the control parameter for stress sensitivity of permeability in porous rock.

3D FINITE ELEMENT METHOD FOR THERMO-POROELASTICITY

At this stage of the work, we develop a 3D finite element program with full poro-thermoelasticity capability [15]. The model uses eight-node hexahedron elements for the displacements u, and eight-node elements for the pore pressure p, and temperature T to improve numerical resolution of displacements. The following variables are approximated using Galerkin's method for u, p, and T:

$$u = N_u \tilde{u} \qquad (20)$$

$$p = N_p \tilde{p} \qquad (21)$$

$$T = N_T \tilde{T} \qquad (22)$$

where the shape functions for the displacement, pore pressure and temperature are N_u, N_p, and N_T, respectively, and nodal variables for displacements, pore pressure and temperature are $\tilde{u}$, $\tilde{p}$ and $\tilde{T}$, respectively. Weak formulations are obtained by substituting Eqns. (20)-(22) to the field Eqn. (10)-(12). For discretizing the time domain, the Crank-Nicolson type approximation is applied. Full description of coupled chemo-thermo-poroelastic finite element formulation and verifications are published by Zhou and Ghassemi (2009) for the 2D case. In convective heat transfer computation, we applied Streamline-Upwind/Petrov-Galerkin (SUPG) method to avoid numerical oscillation [17].

Three-dimensional poro-elastic stress analysis has been carried out using pressurization of the mid-section of the well by a fluid. Results show that effective radial stress distributions are similar to 2D plane-strain case but induced effective tangential stress distributions are different because of the influence of induced vertical stress around injection zone and pore pressure distributions which flow in x-, y-, and z-directions (Fig 1).
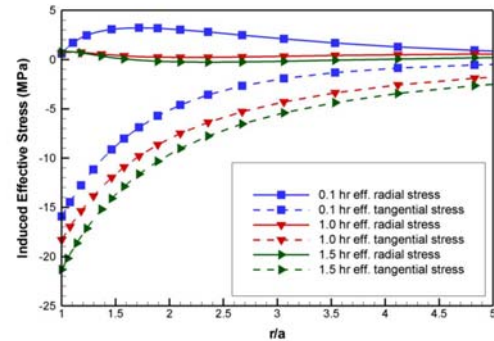

Figure 1: Injection-induced effective radial and tangential stress variation with respect to time. Injection pore pressure is 10 MPa.

Numerical Implementation of Damage Theory

Theory of damage mechanics has been implemented in the 3D finite element code described above. According to the experimental results from Park et al. and Tang et al. [18, 6-7], stresses show a rapid decrease which is related to the softening regime after rock failure.
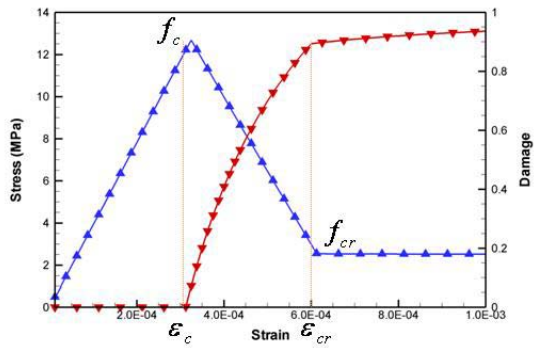
Figure 2: Finite element simulations of compressive triaxial test. Blue line: strain-stress relationships. Damage variable(Red line) evolves after rock failure.
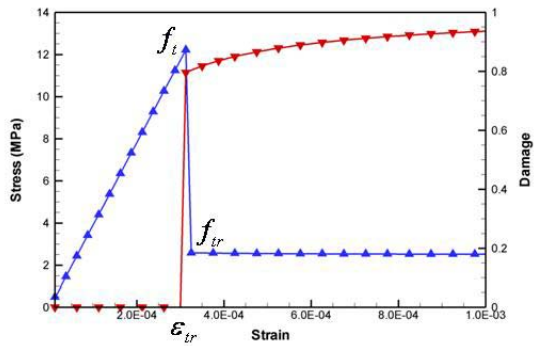

Figure 3: Finite element simulations of tensile triaxial test for comparison of shear-failure damage model. Blue line: strain-stress relationships. Red line: Damage variable
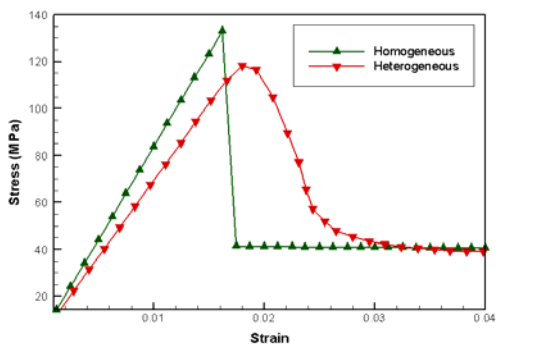

Figure 4: Finite element simulations of a triaxial test. Green line: strain-stress relationships with homogeneous Young's modulus. Damage variable evolves after rock failure; Red line: results from the heterogeneous Young's modulus.

We first performed a number of simulations (of triaxial compression tests) to find the material parameters for the residual strength which determines the level of softening in the damage phase. By comparing the strain-stress behavior and permeability change with experimental data in [18, 6-7], we selected the optimum parameters for permeability ζ_d , β_d , and the cohesive strength in Mohr-Coulomb failure criterion. The simulations involved axisymmetric analysis using 400 elements and 1317 nodes. The aspect ratio (width to height) for the domain used in the triaxial test simulations was 1:4; the confining stresses were applied in the lateral side at the level of experimental conditions (10 MPa).

Fig 2-3 show finite element results of stain-stress behavior for shear and tensile failure. The results show a linear strain-stress behavior in elastic phase, however, the stress drops to its residual stress of the softening regime in damage phase. This damage model has advantages to control stress drop from the peak stress to residual stress, and the value of residual stress with respect to strain variations. To simulate more realistic triaxial test, we considered heterogeneity of modulus using Weibull distribution function which is widely used in a geomechanics simulation to depict heterogeneity of rock. The heterogeneous results are presented in Fig 4 that stress-strain curve is varied smoothly.

NUMERICAL EXAMPLES

3D Simulation of Cold-Water Injection

In this section, we present numerical examples for hydraulic fracturing experiments under the influence of different far-field stress while taking into account fluid and temperature variations around a wellbore.

Before conducting large reservoir simulations, we tested a small simulation domain consisting of a 3D block of rock with dimensions of $10 \times 10 \times 5$ m^3 (Fig. 5) with a 0.2 m injection interval. We use eight-noded hexahedron element for displacements and 8-nodes for pore pressure and temperature. All reservoir properties are represented in Table 2 for granite reservoir. The permeability in the maximum far-field stress direction (x-direction) is 5 times higher than that in the minimum far-field stress direction (y-direction). The vertical permeability value is assumed to be 10% of the permeability in the minimum far-field stress direction. In this example, the maximum horizontal stress is 30 MPa (x-direction), minimum horizontal stress is 20 MPa (y-direction), and the vertical stress is 10 MPa (z-direction). The injection pressure starts at 13 MPa and is increased at 0.5 hr intervals until it reaches 20 MPa.
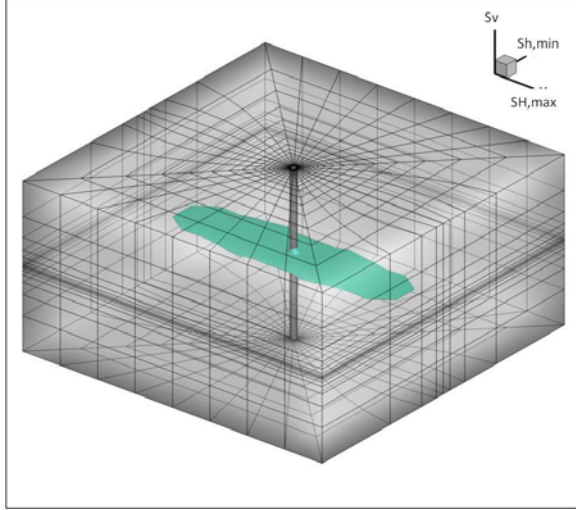
Figure 5: Iso-surface (20%) of injection-induced damage variable for the case when the minimum in-situ stress is S_v.

Table 2: Material properties used in simulations.

Young's modulus, E	10 GPa
ν, ν_u	0.22, 0.46
Skempton's coefficient, B	0.92
Permeability, k	0.001 md
Porosity, ϕ	0.30
Fluid mass density, ρ_f	1111 kg/m^3
Fluid viscosity, η	3.0×10^{-4} Pa·s
Thermal expansion coefficient of solid , α_m and fluid α_f	1.8×10^{-5} K^{-1} 3.0×10^{-4} K^{-1}
Thermal diffusivity, c^T	1.6×10^{-6} m^2/s
Friction angle, ϕ_f	30 °
Cohesive force, c_f	100 MPa
Material constant, ζ_d	100
Material constant, β_d	5.0×10^{-8}

The permeability and pore pressure distributions in the fracture zone are represented in Fig. 6. Note that axial stress (σ_{zz}) distribution (Fig. 7) contributes to failure around the wellbore, along with the tangential stress. It is observed in our fracture simulation that damaged area (micro-crack & void growth area) becomes sharper when damage variable convergences are satisfied. Also, anisotropic permeability model under anisotropic far-field stress shows more realistic results since fluid injection plays an important role in this process and its simulation.
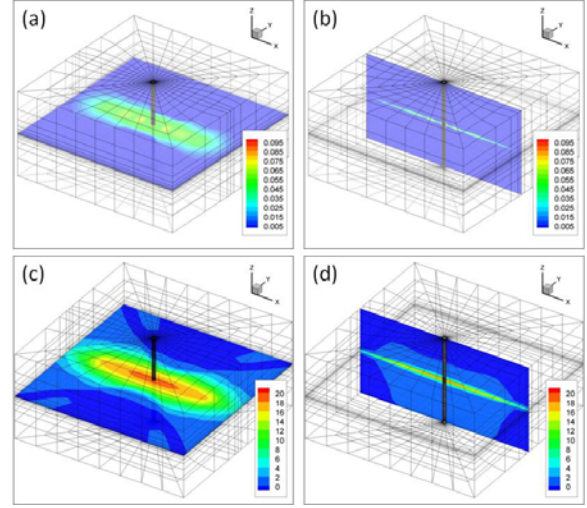

Figure 6: Cross sectional view of permeability and pore pressure distributions. Results are for a time of 6 hrs. Permeability distributions: (a) and (b); pore pressure distributions: (c) and (d). See Table 2 for units.
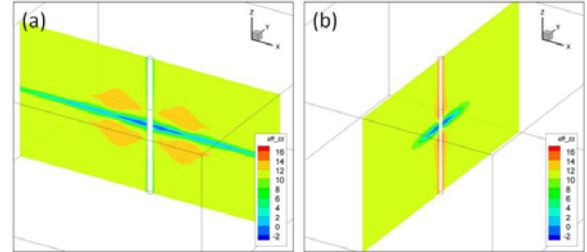

Figure 7: Cross sectional view of effective axial (σ_{zz}) stress distributions at 6 hrs. Cross sectional view for maximum horizontal direction is plotted in (a) and minimum horizontal directions are plotted in (b).

After carrying out small reservoir geomechanical simulations, we conducted large scale reservoir simulations using a large mesh with 83,232 8-noded hexahedron elements for a reservoir size of 240×120 ×150 m^3 as shown in Fig. 8. We tested three different far-field stress regimes: strike-slip: ($S_{H, max}$ = 30 MPa, $S_{h, min}$ = 10 MPa, S_v = 20 MPa), horizontal far-field stress as the minimum in-situ stress; thrust ($S_{H, max}$ = 30 MPa, $S_{h, min}$ = 20 MPa, S_v = 10 MPa), vertical far field stress as the minimum stress component; and normal faulting regime ($S_{H, max}$ = 20 MPa, $S_{h, min}$ = 10 MPa, S_v = 30 MPa), the vertical far field stress as the maximum in-situ stress component. All reservoir properties are the same as the previous simulations, and permeability anisotropy is oriented according to the far-field stress direction, for example, $k_{h,min}$ = 0.1×10^{-3} md, $k_{H, max}$ = 10×10^{-3} md, k_v = 1×10^{-3} md are applied for strike-slip regime, $k_{h,min}$ = 1×10^{-3} md, $k_{H, max}$ = 10×10^{-3} md, k_v = 0.1×10^{-3} md for thrust regime, and $k_{h,min}$ = 0.1×10^{-3} md, $k_{H, max}$ = 1.0×10^{-3}

md, $k_v = 10 \times 10^{-3}$ md are applied for normal fault regime.

Table 3: *Reservoir properties used in three-dimensional diulations.*

	Case 1 (Strike-slip)	Case 2 (Thrust)	Case 3 (Normal)
$S_{H, max}$	30 MPa	30 MPa	20 MPa
$S_{h, min}$	10 MPa	20 MPa	10 MPa
S_v	20 MPa	10 MPa	30 MPa
$k_{H, max}$	0.1×10^{-3} md	1×10^{-3} md	1×10^{-3} md
$k_{h, min}$	10×10^{-3} md	10×10^{-3} md	0.1×10^{-3} md
k_v	0.1×10^{-3} md	0.1×10^{-3} md	10×10^{-3} md
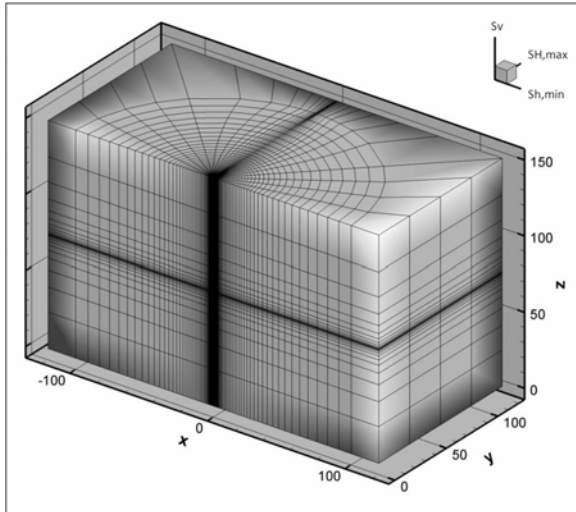
Figure 8: *Mesh used in simulation; $S_{H,max}$ represents maximum horizontal stress, $S_{h,min}$ is the minimum horizontal stress, and S_v is vertical stress.*

In these simulations, damage propagation caused by fluid injection was investigated in relation to the in-situ stress regime. The first case was when the minimum in-situ stress is horizontal (Case 1). The injection interval zone is 2 m and injection pressure begins at 8 MPa and is increased at 2.5 MPa increments every 0.5 hr until it reaches 32 MPa. Fluid injection causes both effective tangential and effective axial stresses to become tensile. These two stress components contribute to tensile principal stress inside the rock. Fig. 9 shows 20% damaged area. Note that damage and fracture propagate vertically and horizontally in this case where the minimum stress is horizontal. Height growth occurs rapidly near the wellbore where the axial stress effects dominate. Away from the wellbore, the in-situ stress controls the manner of damage zone propagation similar to hydraulic fracture. The effective axial stress and pore pressure distributions are shown in Fig. 10.
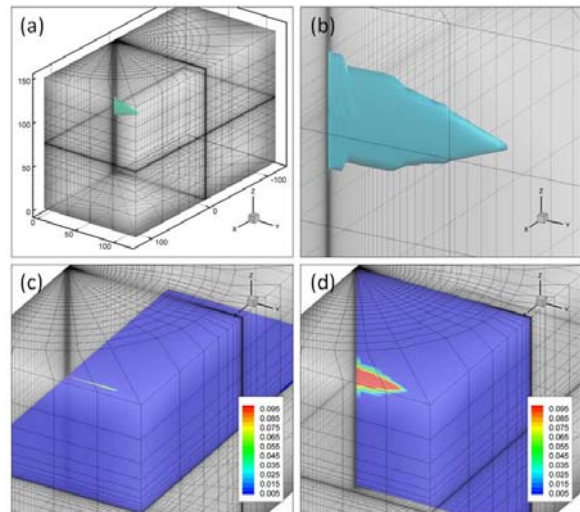

Figure 9: *Damage and permeability distributions for minimum horizontal far-field stress at 12 hrs. 20 % damage of iso-surface is plotted in (a) and (b) is magnified image. Cross sectional view of permeability distributions are illustrated in (c) and (d).*
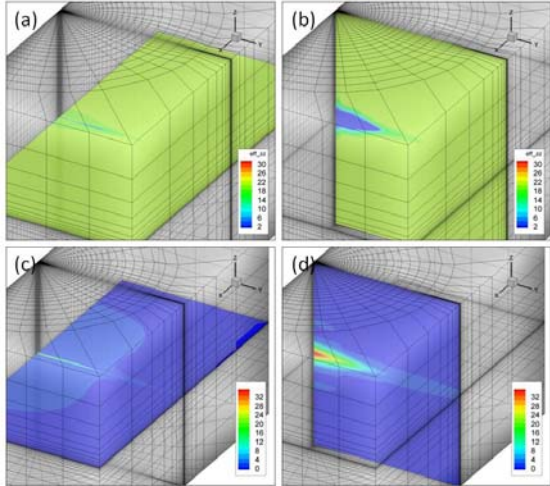
Figure 10: *Effective vertical stress and pore pressure distributions for minimum horizontal far-field stress at 12 hrs. Cross sectional views of effective vertical stress are in (a) and (b) and pore pressure distributions are in (c) and (d), respectively.*
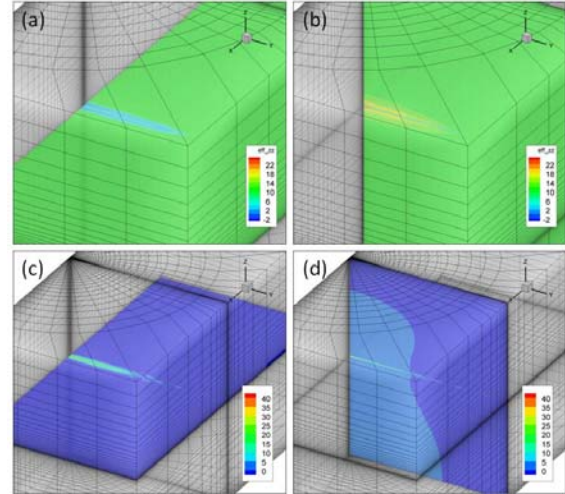
For the Case 2, vertical minimum in-situ stress regime, the injection interval zone is 0.2 m and the pressure is prescribed to begin from 20 MPa and is increased at 2.5 MPa at 0.5 hr until it reaches 42 MPa. Fig. 11 shows fluid induced 20% damaged area and the permeability distribution. Results show that injection induced damage and fractured area propagate horizontally. Pore pressure and stress distribution with damage evolution around a wellbore as shown in Fig. 12.
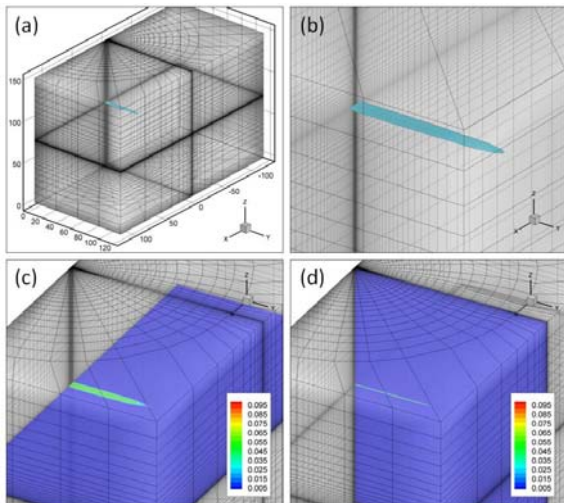

Figure 11: *Damage and permeability distributions for minimum vertical far-field stress at 6 hrs. 20 % damage of iso-surface is plotted in (a) and (b) is magnified image. Cross sectional view of permeability distributions are illustrated in (c) and (d).*
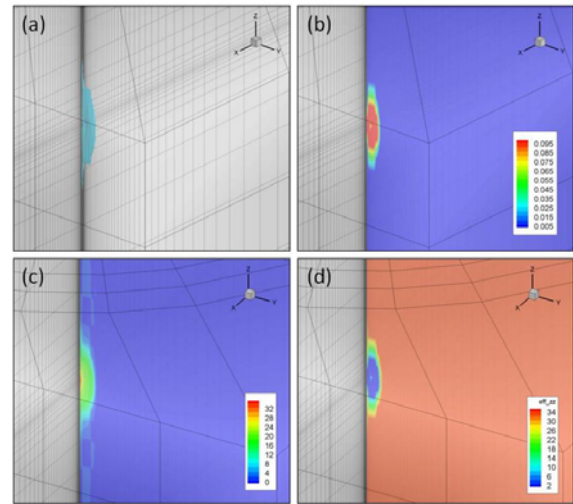

Figure 12: *Effective vertical stress and pore pressure distributions for the case when vertical stress is the far-field minimum stress, at 6 hrs. Cross sectional views of effective vertical stress are in (a) and (b) and pore pressure distributions are in (c) and (d), respectively.*

Figure 13: *Distributions of damage, permeability, pore pressure, and effective vertical stress for the case when vertical stress is the far-field maximum stress, at 6 hrs. 20% damage of iso-surface is plotted in (a) and cross sectional views of permeability is in (b). Pore pressure and effective vertical stress distributions are in (c) and (d), respectively.*

For the Case 3, vertical stress as the maximum far field stress, the same injection rate conditions of Case 1 are used for the comparison of normal fault regime with strike-slip regime (Case 1). Only different properties are far-field stress distribution and permeability anisotropy because of maximum far-field stress directions are varied from y-direction to z-direction. Results show a stronger tendency for the

induced damage and fractured zone to propagate vertically; however as shown in Fig 13, the damage area is smaller (for the same injection rate of Case 1) because of the influence of large vertical far field stress. The different geometry of the failure plane for the case of $S_{h,min}$ and S_v as the minimum in-situ stress component can be attributed to different patterns of fluid and stress distribution in each case. In this simulation, it is observed that effective axial stress caused by fluid injection is the main contributor to tensile failure across the wellbore for case 1 and case 3 ($S_{h,min}$ as minimum). However, in the case of S_v as the minimum stress, the effective axial stress is not significant compared to the minimum $S_{h,min}$ and the wellbore hoop stress which serve to propagate the damage. We observe that a higher injection pressure is needed to generate the fracture plane in the homogeneous rock case, when S_v is the minimum in-situ stress rather than $S_{h,min}$ because of the effective stress contributions for tensile failure. This is reasonable since there is additional hoop tensile stress when the fracture in initiated in a vertical plane (as opposed to only axial).
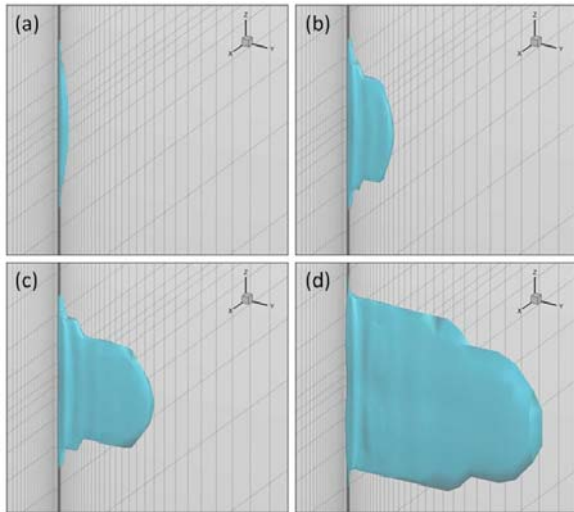

Figure 14: Iso-surface 20% damage plot of three-dimensional damage propagation with respect to time under horizontal far-field stress as the minimum: (a): 0.5hr, (b): 1 hr, (c): 1.2 hr, (d): 1.5 hr

The variation of damage propagations with time for the strike-slip, thrust and normal fault regimes are illustrated in Fig. 14-16 for comparison.
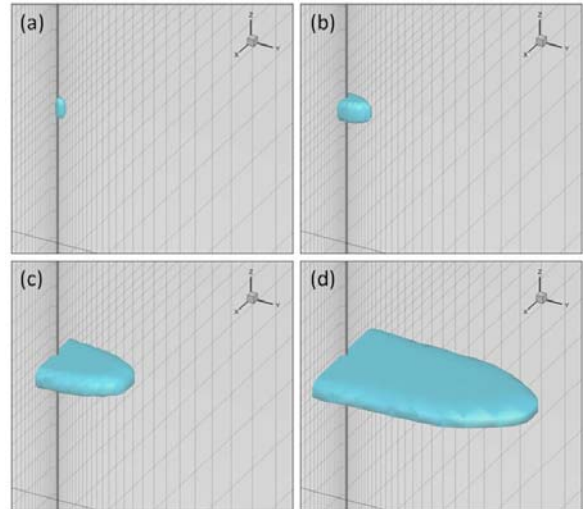

Figure 15: Iso-surface 20% damage plot of three-dimensional damage propagation with respect to time under vertical far-field stress as the minimum: (a): 1 hr, (b): 1.2 hr, (c): 1.5 hr, (d): 1.9 hr.
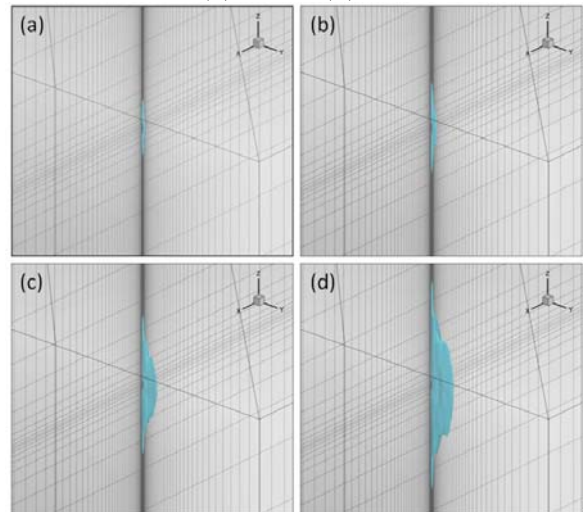

Figure 16: Iso-surface 20% damage plot of three-dimensional damage propagation with respect to time under vertical far-field stress as the maximum: (a): 1.5 hr, (b): 2 hr, (c): 4 hr, (d): 8 hr.

Hydraulic fracturing with cold water injection has been illustrated in Fig 17. Initial reservoir temperature is 200 °C and cold water temperature is 65 °C. Injection pressure is maintained 35 MPa for 6 hr which starts from 8 MPa. Both fluid injection and temperature difference contribute fracture propagation. In this simulation, we assume hydraulic fracture (macro crack) as 90% damage. Results show that 90% damage zone length is 24 m, height is 8 m, and average thickness near the well 10 cm. Note that temperature distribution is influenced by fluid flow which is related with convective heat transfer but transfer rate is very slow.
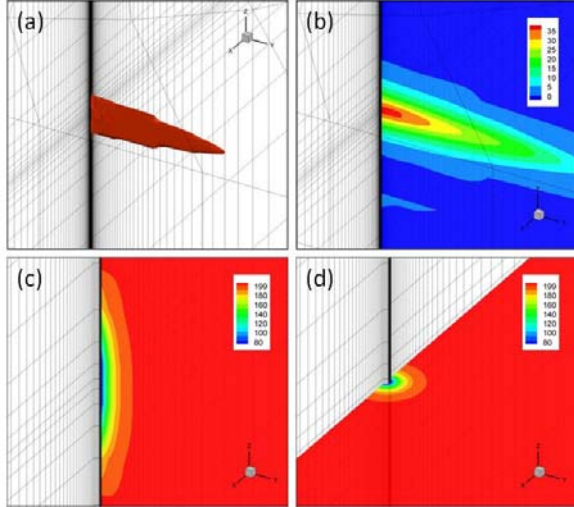
Figure 17: *Plot for hydraulic fracturing zone (90% damaged area) in horizontal stress as the minimum (a), and pore pressure distribution (b). Different planes view of temperature distributions in (c) and (d). All results have the same time step at 6 hr.*

Three-Dimensional Simulation of Injection-Induced Micro-Seismicity

In this section, we consider induced micro-seismicity simulations with damage evolution. It is assumed that seismic events are generated when the effective rock stress reaches the level prescribed by the failure criterion (Mohr-Coulomb) as fluid infiltrates the rock and stresses change. The simulation mesh is the same in the previous homogeneous three-dimensional simulations. However, heterogeneities of modulus and permeability are considered using Weibull distribution functions. The initial modulus and permeability distributions are illustrated in Fig. 18. As before, three different far-field stress regimes are tested one with horizontal stress as the minimum, another with vertical stress as the minimum and the other with vertical stress as the maximum. To investigate the permeability and far-filed stress relationship, we also considered two different permeability models namely (1) reservoir permeability properties are highly related to the far-field stress (anisotropic permeability) and permeability are independent of the far-field stress (isotropic permeability). Details of reservoir properties are described in Table 4. In the case of anisotropic permeability, we simply assumed a permeability that is 10 times higher in the maximum in-situ stress direction and 10 times lower in minimum in-situ stress direction.

Table 4: *Reservoir properties used in three-dimensional heterogeneous simulations.*

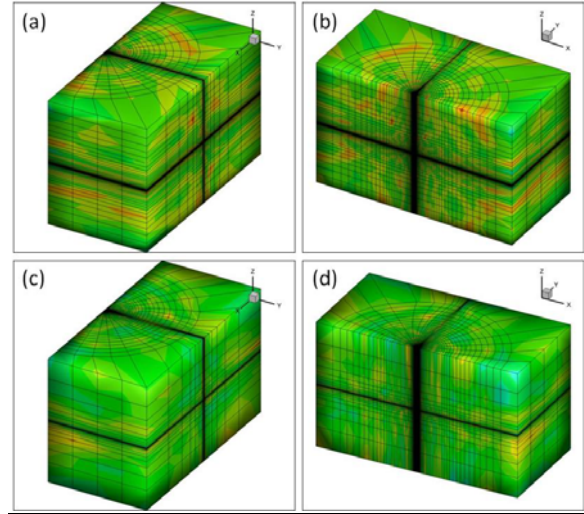|	Case 1	Case 2	Case 3	Case 4	Case 5	Case 6
Stress regime	Strike-slip		Thrust		Normal	
E	10 GPa (n=1.5)		10 GPa (n=1.5)		10 GPa (n=1.5)	
K, md (n=1.5)	10^2	$k_{max}=10\times10^2$ $k_{min}=0.1\times10^2$ $k_v=1.0\times10^2$	10^2	$k_{max}=10\times10^2$ $k_{min}=1.0\times10^2$ $k_v=0.1\times10^2$	10^2	$k_{max}=1\times10^2$ $k_{min}=0.1\times10^2$ $k_v=10\times10^2$
C_0	100 MPa (n=2)		100 MPa (n=2)		100 MPa (n=2)	
T_0	5 MPa (n=2)		5 MPa (n=2)		5 MPa (n=2)	

Figure 18: *Initial heterogeneous modulus is plotted in (a), (b) and permeability distribution is presented in (c), (d).*

The resulting seismic events and permeability distributions are plotted in Fig. 19 for different reservoir permeability. Fig. 19 (a) shows the seismic events in time for the conditions of isotropic permeability with minimum horizontal far-field stress. Fig. 19 (b) shows a plot for the same far-field stress conditions and injection rate but with anisotropic permeability. It is observed the seismic events are scatted broadly when permeability is isotropic since there are no significant differences in fluid sweep velocities in the x-, y-, and z-directions. However, in the case of anisotropic permeability, seismic events are highly localized because fluid invasion is focused in the maximum far-field stress direction and this leads to localized seismic events. Same conditions are simulated for the minimum vertical far-field stress case (Fig. 20). It is similarly observed that broad distributed seismic events occur under isotropic permeability conditions, and scattered

localized events are observed in the anisotropic permeability case. Vertical stress as the maximum has been plotted in Fig. 21. Note that same injection conditions are used for both stress regime simulations. Results show that for the normal faulting case, the induced-seismicity does not propagate and stabilizes earlier because vertical stress is higher compared to the thrust regime where a higher injection rate is needed to generate tensile failure for fracture propagation in the vertical direction. It is worth pointing out that the smaller grey points show the distribution of micro-seismic events as a result of the far-filed stresses and might be interpreted as background values.
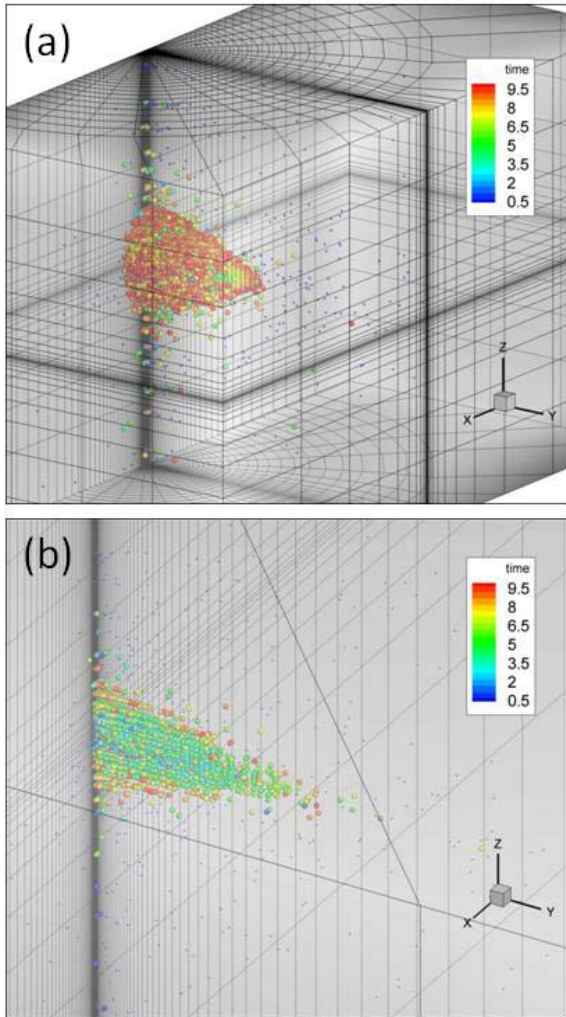

Figure 19:   *Predicted micro-seismic events after 10 hrs of pumping for the case of horizontal stress being the minimum far-field stress: (a) the case of isotropic permeability and (b) anisotropic permeability.*
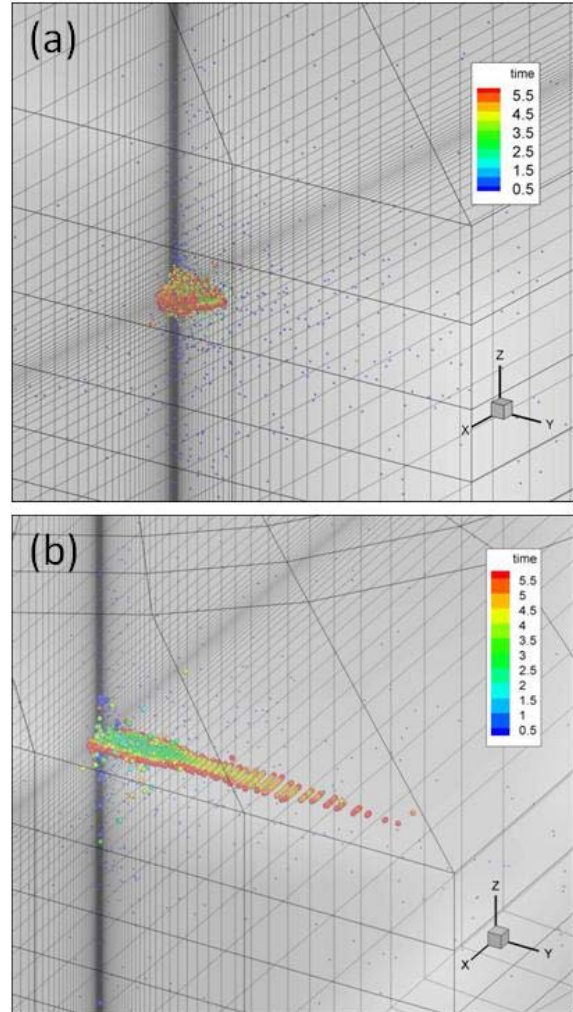

Figure 20:   *Micro-seismic events after 6 hrs of pumping for the case that the vertical stress is the minimum far-field. (a) the case of isotropic permeability and (b) anisotropic permeability.*
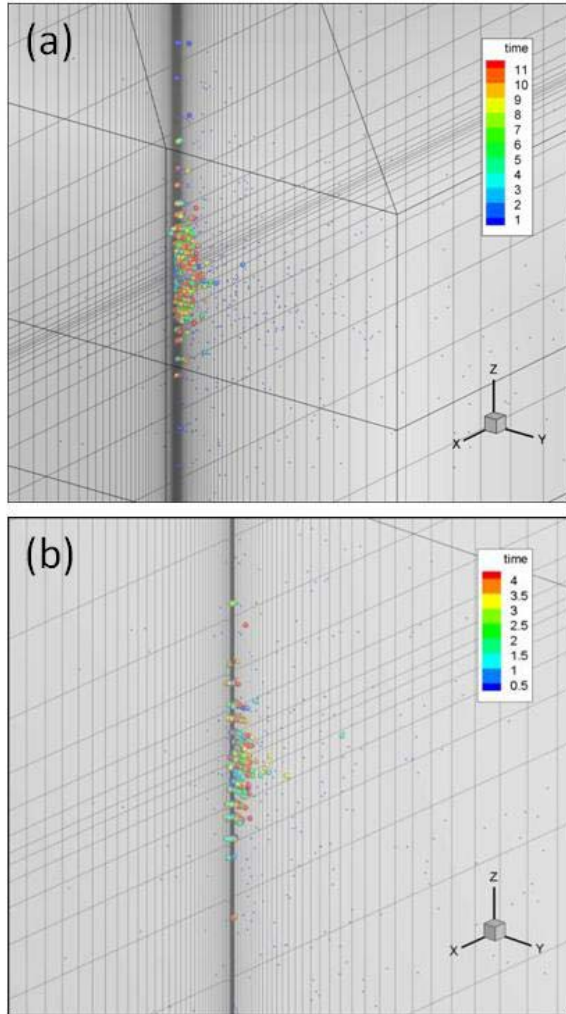
Figure 21: Micro-seismic events after 6 hrs of pumping for the case that the vertical stress is the maximum far-field. (a) the case of isotropic permeability and (c) anisotropic permeability.

CONCLUSIONS

A three-dimensional fully coupled finite element method has been developed for modeling damage-induced stress variations and permeability change along with induced seismicity. The model was used to simulate a number of synthetic hydraulic fracturing experiments for different stress regimes. Vertical damage propagation observed when the horizontal far-field stress is the minimum in-situ stress component, whereas horizontal damage propagation is observed when the vertical far field stress as the minimum. Comparison between the results for the strike-slip and normal faulting regimes using the same injection rate show that damage area is smaller for the latter case. Also, it is observed that higher injection pressure is needed to generate a horizontal fracture plane in a thrust faulting regime compared to the vertical fracture plane in strike-slip stress regime. This is because of the effective stress contributions to tensile failure. Realistic patterns of micro-seismicity have been generated for these stimulation experiments. Results show the significant roles of stress state and initial rock permeability in the resulting pattern. The results of this study indicate that the finite element method with damage can be used to model reservoir stimulation and induced seismicity. Effort is ongoing to simulate damage propagation and induced seismicity under different injection rates, various permeability structures involving faults, and different in-situ stress regimes for small and large size reservoirs and to compare results with available lab and field experiments.

REFERENCES

1. Biot M. A. (1941), "General theory of three-dimensional consolidation", *J. Appl. Phys*, **12**, 155–164

2. Ghassemi A. and A. Diek. (2002), "Poro-thermoelasticity for swelling shales", *J. Pet. Sci. Eng.*, **34**,123–135.

3. Kachanov L. M. (1958), "Time of the rupture process under creep conditions", *Isv. Akad. Nauk SSR. Otd Tekh. Nauk.*, **8**, 26-31

4. Mazars J. (1986), "A description of micro- and macroscale damage of concrete structures", *Eng. Fracture. Mech.*, **25**, 729-737

5. Simakin A. and Ghassemi A. (2005), "Modelling deformation of partially melted rock using a poroviscoelastic rheology with dynamic power law viscosity", *Tectonophysics*, **397**, 195–209.

6. Tang C.A., Tham L.G., Lee P.K.K., Yang T.H. and Li L.C. (2002), "Coupled analysis of flow, stress and damage (FSD) in rock failure", *Int. J. Rock Mech. & Min. Sci.,* **39**, 477–489.

7. Li L.C, Tang C.A., Tham L.G., Yang T.H. and Wang S.H. (2005), "Simulation of multiple hydraulic fracturing in non-uniform pore pressure field", *Adv. Mater. Res.*, **9**, 163–172.

8. Selvadurai A. P. S. (2004), "Stationary damage modeling of poroelastic contact", *Int. J. Solids and Structures*, **41**, 2043-2064.

9. Shipping L., Yushou L., Yi L., Zhenye W. and Gang Z. (1994), "Permeability-strain equations corresponding to the complete stress-strain path of Yinzhuang Sandstone", *Int. J. Rock Mech. Min. Sci. Geomech. Abstr.*, **31**, 383-391.

10. Kiyama T., Kita H., Ishijima Y., Yanagidani T., Akoi K. and Sato T. (1996), "Permeability in anisotropic granite under hydrostatic compression and tri-axial compression including post-failure region", *Proc. 2nd North Amer. Rock Mech. Symp.*, 1643-1650.

11. Coste F., Bounenni A., Chanchole S. and Su K. (2001), "A method for measuring hydraulic and hydromechanical properties during damage in materials with low permeability", *Thermohydromechanical Behaviour of Deep Argillaceous Rock*, The Netherlands. 109-116.

12. Zoback M. D. and Byerlee J. D. (1975), "The effect of micro-crack dilatancy on the permeability of westerly granite", *J. Geophys. Res.*, **80**, 752-755.

13. McTigue, D.F. (1986), "Thermoelastic response of fluid-saturated porous rock", *J. Geophys. Research,* **91(B9)**, 9533-9542.

14. Palciauskas W. and Domenico PA. (1982), "Characterization of drained and undrained response of thermally loaded repository rocks", *Water Res. Res.*, **18**, 281–290.

15. Zhou X. and Ghassemi A. (2009), "Finite element analysis of coupled chemo-poro-thermo-mechanical effects around a wellbore in swelling shale", *Int. J. Rock Mech. & Sci.*, **46**, 769-778.

16. Smith I. M. and Griffiths D. V. (2004), "Programming the finite element method", John Wiley & Son, 4th edition.

17. Heinrich J. C. and Pepper D. W. (1999), "Intermediate finite element method: fluid flow and heat transfer applications", Taylor & Francis.

18. Wang J. A. and Park H. D. (2002), "Fluid permeability of sedimentary rock in a complete stress-strain process", *Eng. Geology*, **63**, 291-300.1.